Mechanism of Photocatalytic CO_2 Reduction by Bismuth-Based Perovskite Nanocrystals at the Gas−Solid Interface

Sumit S. Bhosale,[†] Aparna K. Kharade,[‡] Efat Jokar,[†,§] Amir Fathi,[†] Sue-min Chang,[‡] and Eric Wei-Guang Diau*,[†,§]

[†]Department of Applied Chemistry and Institute of Molecular Science, National Chiao Tung University, 1001 Ta-Hsueh Road, Hsinchu 30010, Taiwan

[‡]Institute of Environmental Engineering, National Chiao Tung University, Hsinchu 30010, Taiwan

[§]Center for Emergent Functional Matter Science, National Chiao Tung University, 1001 Ta-Hsueh Road, Hsinchu 30010, Taiwan

Ⓢ *Supporting Information*

ABSTRACT: We report here a series of nontoxic and stable bismuth-based perovskite nanocrystals (PeNCs) with applications for photocatalytic reduction of carbon dioxide to methane and carbon monoxide. Three bismuth-based PeNCs of general chemical formulas $A_3Bi_2I_9$, in which cation $A^+ = Rb^+$ or Cs^+ or $CH_3NH_3^+$ (MA^+), were synthesized with a novel ultrasonication top-down method. PeNC of $Cs_3Bi_2I_9$ had the best photocatalytic activity for the reduction of CO_2 at the gas−solid interface with formation yields 14.9 μmol g^{-1} of methane and 77.6 μmol g^{-1} of CO, representing a much more effective catalyst than TiO_2 (P25) under the same experimental conditions. The products of the photocatalytic reactions were analyzed using a gas chromatograph coupled with a mass spectrometer. According to electron paramagnetic resonance and diffuse-reflectance infrared spectra, we propose a reaction mechanism for photoreduction of CO_2 via Bi-based PeNC photocatalysts to form CO, CH_4, and other possible side products.
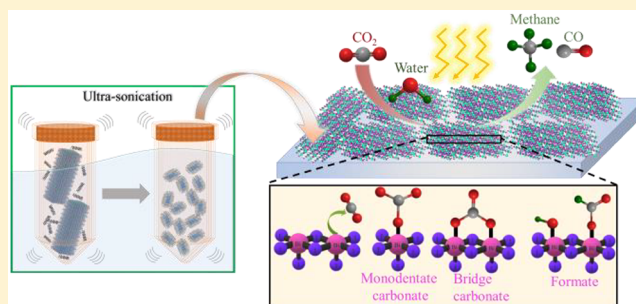
INTRODUCTION

Because the demand for energy is strong, the rapidly increasing consumption of limited fossil fuels causes depletion of these traditional sources of energy and releases CO_2 into the atmosphere, resulting in global warming. Among all solutions to decrease the amount of CO_2 in the atmosphere, the conversion of CO_2 into fuels through artificial photosynthesis seems to be a promising approach. Much effort has been exerted to develop effective, environmentally compatible, and stable photocatalysts. Various semiconductors with varied chemical and crystal structures have been investigated for the photocatalytic reduction of CO_2.[1−3] The size and shape of the catalyst particles are two key factors for the catalytic performance, which have been widely studied. On decreasing the size of the catalyst particle to a nanometer scale, new catalytic function has appeared with great performance.[4]

Organic−inorganic hybrid perovskites are promising semiconductors with outstanding optical and electrical properties that have been employed in applications such as solar cells,[5−7] light-emitting diodes,[8−12] photon detectors,[13,14] and lasers,[15−17] among others.[18] The popularity of the use of perovskites is attributed to their tunable optoelectronic properties, cost effectiveness, and solution-based fabrication. On decreasing the size of perovskite materials to form perovskite nanocrystals (PeNCs), the photoluminescence quantum yield (PLQY) becomes enhanced with the advantages of a large surface area and excellent stability. Lead (Pb)-based PeNCs have been studied for photocatalysis.[19,20] PeNCs of high quality can be fabricated with hot injection,[21] ligand-assisted reprecipitation (LARP),[22] and top-down methods.[23] $CsPbBr_3$,[20] a hybrid $CsPbBr_3/GO$[19] composite, and a $CsPbBr_3$/metal−organic framework (MOF)[24] were utilized for the photocatalytic reduction of CO_2. Although these photocatalysts demonstrated effective CO_2 conversion, the toxicity of lead to human life due its high solubility in water limits their potential for widespread application. An alternative option to replace of lead is tin (Sn) in PeNCs, but tin-based PeNCs suffer instability and small PLQY.[25] In contrast, bismuth (Bi)-based PeNCs of general chemical formula $A_3Bi_2I_9$ (cation A can be K^+, Rb^+, Cs^+, or methylammonium MA^+) provide a nontoxic and chemically stable alternative for photocatalytic applications.[26] Bismuth perovskites have been applied as solar cells; the best $Cs_3Bi_2I_9$ device attained a power conversion efficiency (PCE) of only 1.09%[27] and for $MA_3Bi_2I_9$ 3.17%.[28] These $A_3Bi_2I_9$ compounds have structures of two types: $K_3Bi_2I_9$ and $Rb_3Bi_2I_9$ have 2D defect-perovskite structures with corrugated layers of
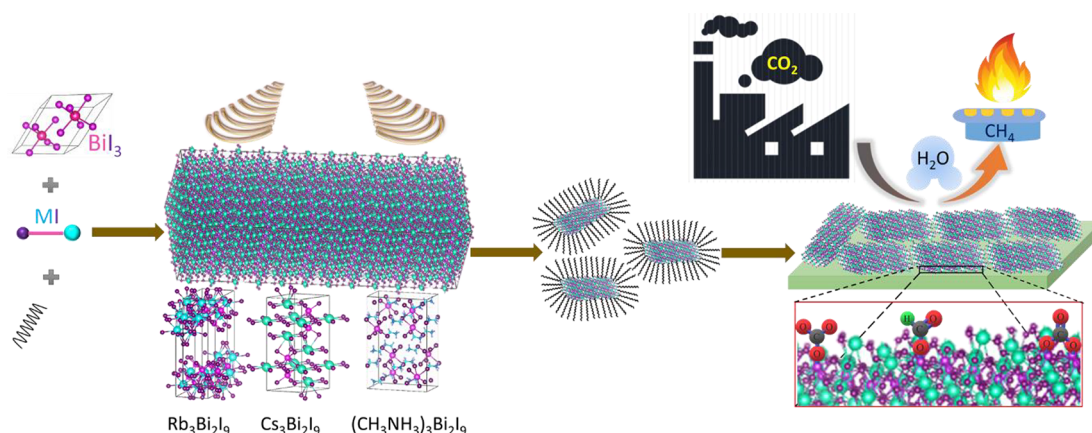
Figure 1. Schematic representation of the top-down method to fabricate bismuth-based perovskite nanocrystals and its application in the solid−gas photocatalytic reduction of carbon dioxide.
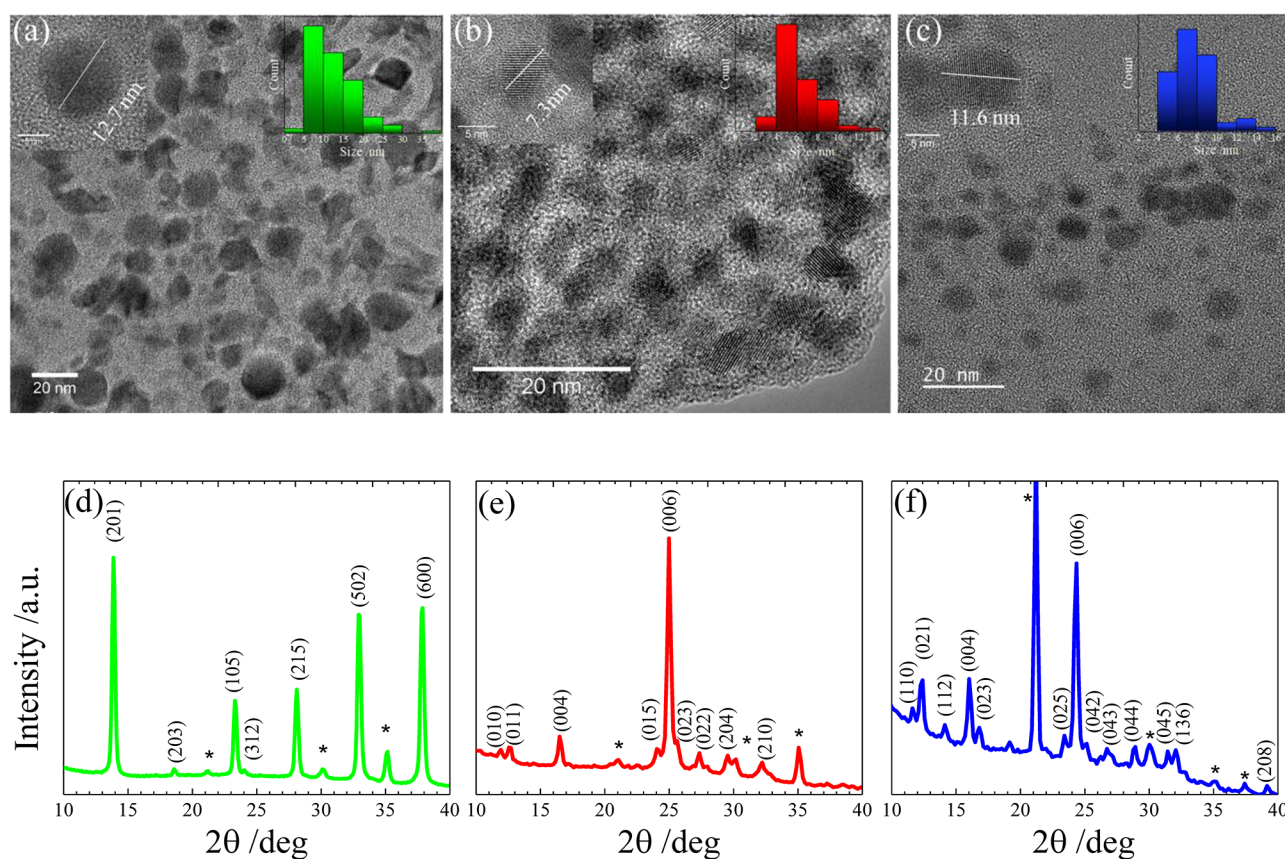

Figure 2. TEM images and size distribution of (a) $Rb_3Bi_2I_9$, (b) $Cs_3Bi_2I_9$, and (c) $MA_3Bi_2I_9$ and X-ray diffraction patterns of (d) $Rb_3Bi_2I_9$, (e) $Cs_3Bi_2I_9$, and (f) $MA_3Bi_2I_9$. Symbol * denotes diffraction signals of the ITO substrate.

corner-connected Bi−I octahedra, whereas $Cs_3Bi_2I_9$ and $MA_3Bi_2I_9$ possess a zero-dimensional structure with isolated $Bi_2I_9^{3-}$ ions forming face-sharing Bi−I octahedra.[29] Although Bi-based PeNCs were synthesized with a LARP method[30,31] with satisfactory stability, the PLQY was still less than that of their Pb-based analogues.

In this work, we applied for the first time a top-down method to synthesize three Bi-based PeNCs, namely, $Rb_3Bi_2I_9$, $Cs_3Bi_2I_9$, and $MA_3Bi_2I_9$, for photoreduction of CO_2 to CO and CH_4 at a gas−solid interface; the synthetic approach is schematically demonstrated in Figure 1. We report here not only a new approach to synthesize Bi-based PeNCs but also a detailed reaction mechanism of CO_2 reduction using halide perovskite PeNCs as photocatalysts. CO_2 was reduced photochemically to generate end products CO and CH_4; the photocatalytic activity of Bi-based photocatalysts shows a trend $Cs_3Bi_2I_9$ > $Rb_3Bi_2I_9$ > $MA_3Bi_2I_9$ ≫ TiO_2. Electron paramagnetic resonance (EPR) and diffuse-reflectance infrared spectra were recorded to explain the effect of the cation in the photocatalytic reaction; on this basis we propose a mechanism of CO_2 reduction with PeNCs. We further show that CO_2 photoreduction follows one of two paths, identifiable through either a formate or carbonate intermediate. The results show
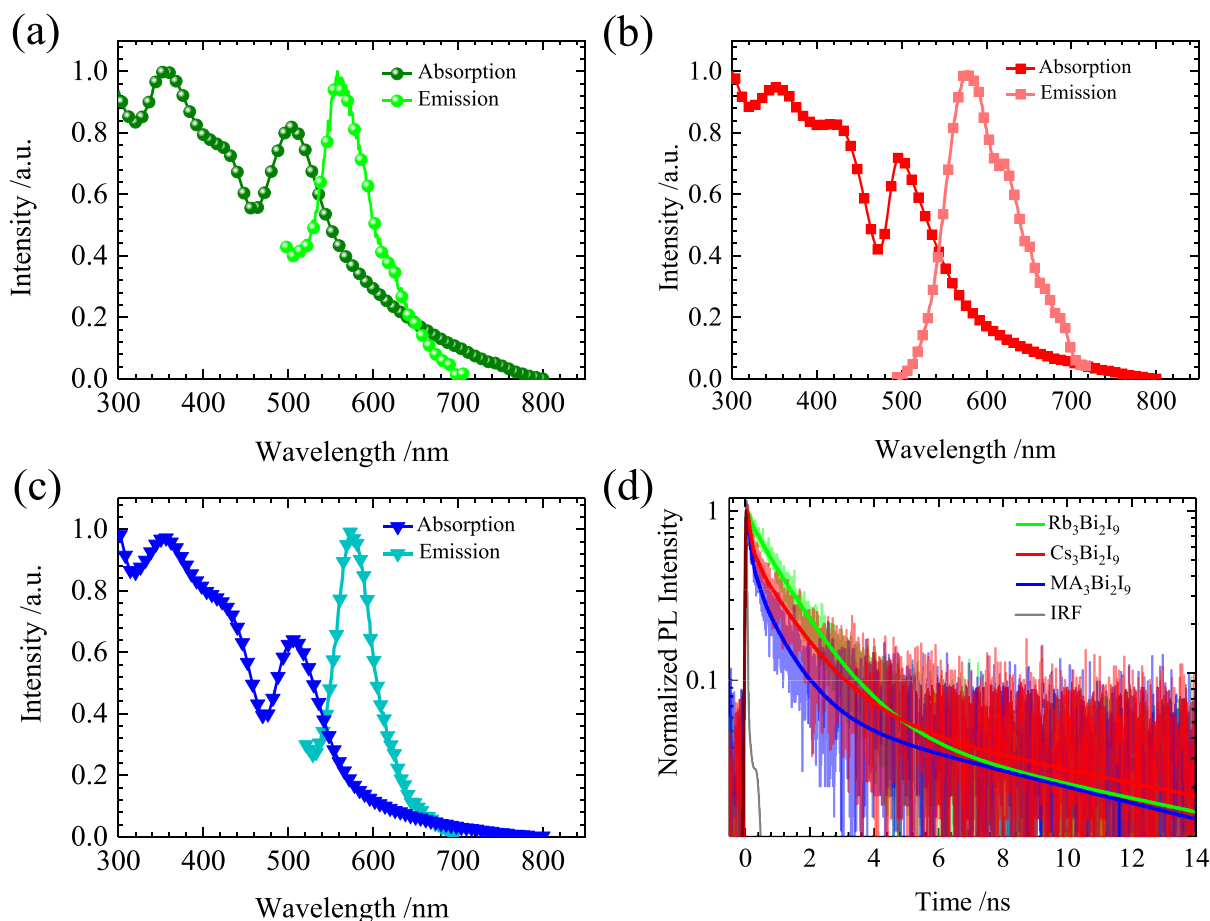
Figure 3. Steady-state absorption and PL spectra of PeNCs: (a) $Rb_3Bi_2I_9$, (b) $Cs_3Bi_2I_9$, and (c) $MA_3Bi_2I_9$; (d) transient PL decay profiles of PeNCs as indicated.
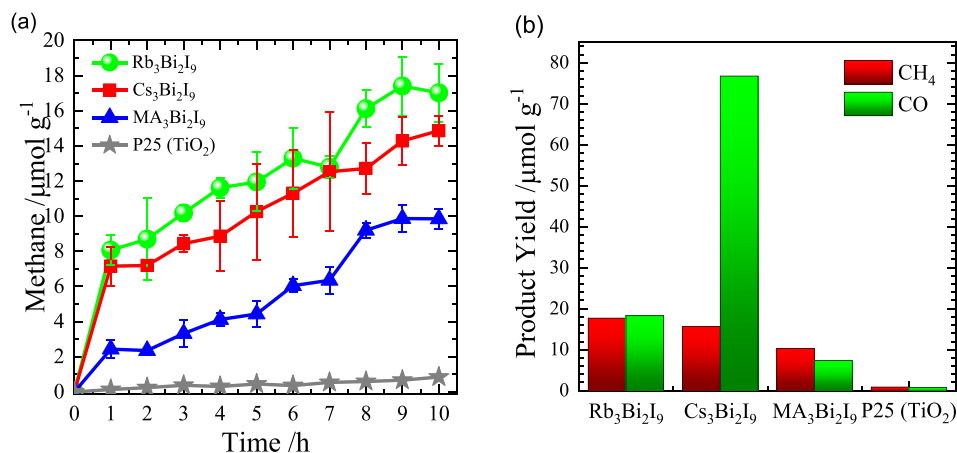

Figure 4. (a) Product yields of methane production with catalysts at each hour of reaction (detected with GC-FID); (b) comparison of production of methane and carbon monoxide during photochemical reaction for 10 h (detected with GC-MS).

that the cation (in site A) and the crystal structure are important factors affecting the catalytic activity.

RESULTS AND DISCUSSION

Although the top-down method was reported for Pb-based PeNC,[23] according to our knowledge this report is the first to describe Bi-based PeNCs produced with an ultrasonic top-down method. Moreover, we used these PeNCs as efficient photocatalysts for CO_2 reduction. Bulk perovskite crystals were formed on simply grinding the precursors (Figure 1) in the presence of dimethylformamide (DMF) (a few drops); the bulk perovskites were fragmented with an ultrasonication method. The obtained PeNCs were protected with oleic acid (OA) and oleylamine (OLA) ligands present in the original precursor solution. As the preparation of PeNC involves irregular breaking of bulk perovskite crystals, the obtained PeNCs have varied shapes and sizes on a nanometer scale. The morphology, crystallinity, and size distribution of PeNCs for
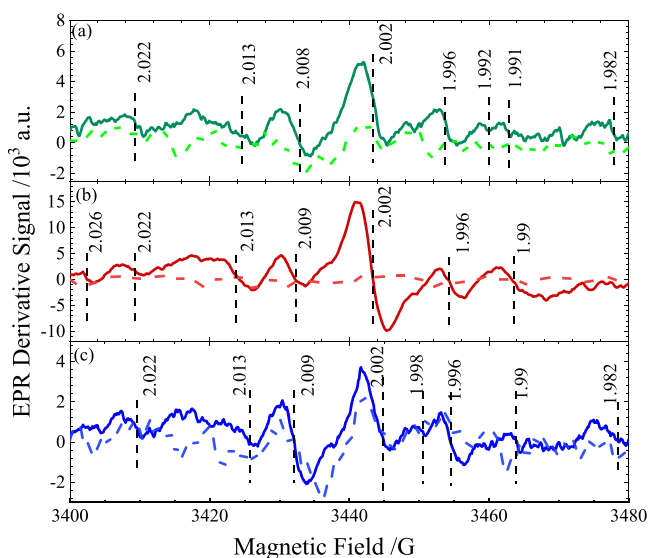
Figure 5. Electron paramagnetic resonance (EPR) spectra of (a) $Rb_3Bi_2I_9$, (b) $Cs_3Bi_2I_9$, and (c) $MA_3Bi_2I_9$ under illumination for 1 h in the absence (solid curves) or presence (dashed curves) of CO_2 and H_2O. The vertical dashed lines show the corresponding g-factor values.

$Rb_3Bi_2I_9$, $Cs_3Bi_2I_9$, and $MA_3Bi_2I_9$ were observed with a transmission electron microscope (TEM), as shown in Figure 2a−c, respectively. The average crystal diameter was 12.6, 6.2, and 7.6 nm for $Rb_3Bi_2I_9$, $Cs_3Bi_2I_9$, and $MA_3Bi_2I_9$ PeNCs, respectively. TEM images in Figure S1, Supporting Information (SI), were used to determine the size distribution.

Powder X-ray diffraction (XRD) patterns for $A_3Bi_2I_9$ (A = Rb^+, Cs^+, and MA^+) PeNCs are shown in Figure 2d−f. XRD patterns were matched with standard XRD data reported for bulk structures.[27,32] $Cs_3Bi_2I_9$ and $MA_3Bi_2I_9$ PeNCs adopt a hexagonal structure of space group $P63/mm$;[27] $Rb_3Bi_2I_9$ has a monoclinic structure of space group $P21/n$.[32] The broad background originated from organic ligands; a slight shift and

peak broadening are attributed to the nanocrystalline nature of the PeNC.[33] The elemental composition was analyzed with X-ray photoelectron spectra (Figure S2, SI); as shown in Figure S2a−c, SI, these data exhibit Bi 4f signals at 159 and 164 eV, C 1s at 185 eV, N 1s at 400 eV, and I 3d at 630 and 618 eV. For the $Cs_3Bi_2I_9$ sample, Cs 3d signals at 726 eV and for the $Rb_3Bi_2I_9$ sample Rb at 112 eV were detected. Carbon, nitrogen, bismuth, and iodine were common to all samples; capping organic ligands contribute to these signals of carbon and nitrogen. As reported elsewhere,[31] for Bi-based PeNCs, the surface composition of bismuth varies with particle size.

The optical properties of PeNCs in colloidal solutions and in spin-coated films were analyzed. The absorption spectra of PeNC solutions show excitonic transitions centered at 504, 498, and 506 nm for $Rb_3Bi_2I_9$, $Cs_3Bi_2I_9$, and $MA_3Bi_2I_9$, respectively (Figure 3). The photoluminescence (PL) spectra of $Rb_3Bi_2I_9$, $Cs_3Bi_2I_9$, and $MA_3Bi_2I_9$ PeNC solutions showed maximum intensities at 558, 578, and 575 nm, respectively. According to optical characterizations of PeNC solid films (Figure S3, SI), their emission spectra show bathochromic shifts from solution samples, indicating an aggregation of PeNCs in thin-film samples, but the PL spectra of PeNCs have two features that indicate the existence of both direct and indirect band gaps near 298 K.[34] To understand the charge-carrier kinetics, we measured transient PL decays; the PeNC samples were excited at 375 nm. The PL decays were monitored at the corresponding emission maxima of the PeNC solutions.

All PL decays were fitted with a triexponential decay function; the corresponding fitting parameters are listed in Table S1, SI. The first decay components (τ_1) are limited to almost the pulse duration for all three samples, but the amplitudes show the order $MA_3Bi_2I_9 > Cs_3Bi_2I_9 > Rb_3Bi_2I_9$. This rapid decay component is attributed to trap-state relaxation.[30] The $Rb_3Bi_2I_9$ sample is hence expected to have fewer bulk trap states inside the PeNC than the other samples according to the trend of the amplitude of τ_1. The second decay component (τ_2) is assigned to recombination of surface
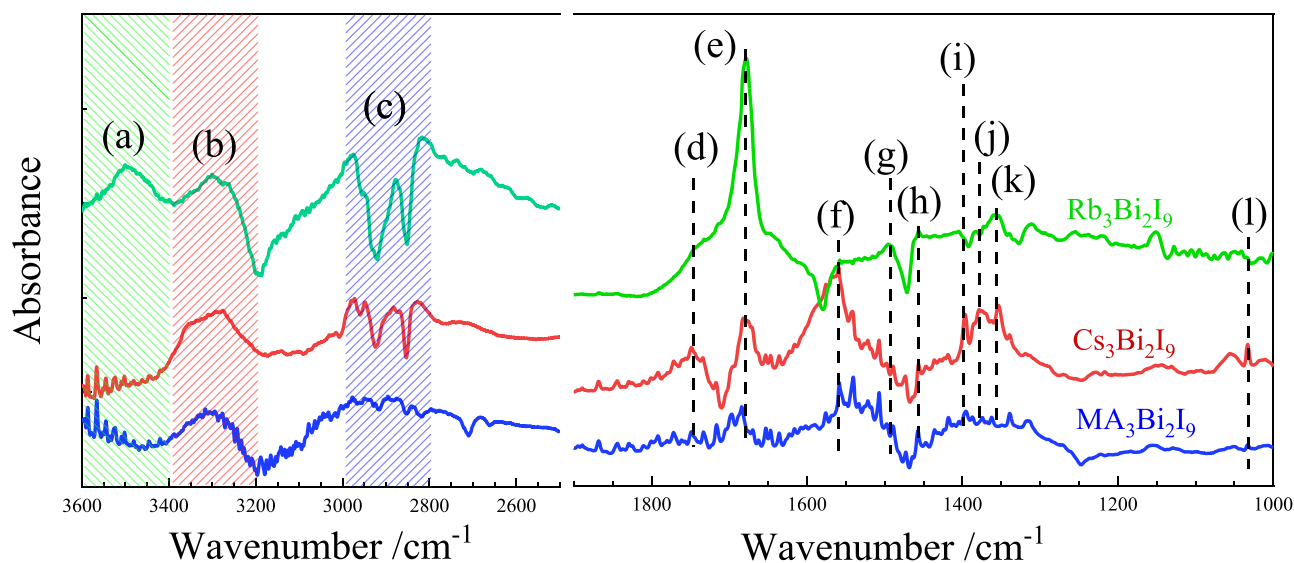
Figure 6. Diffuse-reflectance infrared spectra of $Rb_3Bi_2I_9$ (blue), $Cs_3Bi_2I_9$ (red), and $MA_3Bi_2I_9$ (black) in the presence of CO_2 and H_2O under illumination for 5 h. Chemical species observed in these spectra are assigned as (a) free −OH, (b) H-bonded −OH, (c and k) formate,[46] (d) bridge carbonate,[47] (e) dioxycarbon anion,[48] (f and i) monodentate carbonate,[47,49,50] (g and j) bidentate carbonate,[51−53] (h) bicarbonate, and (l) methoxy.[46]

(1) Monodentate Channel

(2) Bidentate Channel

(3) Formation of methane from formate

(4) Side reactions

Figure 7. Plausible mechanism of photoreduction of CO_2 via Bi-based PeNC catalysts.

defects.[31] τ_2 showed the trend $Rb_3Bi_2I_9 \sim Cs_3Bi_2I_9 > MA_3Bi_2I_9$ with the corresponding amplitudes showing the trend $Rb_3Bi_2I_9 > Cs_3Bi_2I_9 > MA_3Bi_2I_9$. The $Rb_3Bi_2I_9$ sample is hence expected to undergo slower recombination of surface defects than the others; the $MA_3Bi_2I_9$ sample might suffer from charge recombination on the surface. The third component (τ_3) might be assigned to the radiative charge recombinat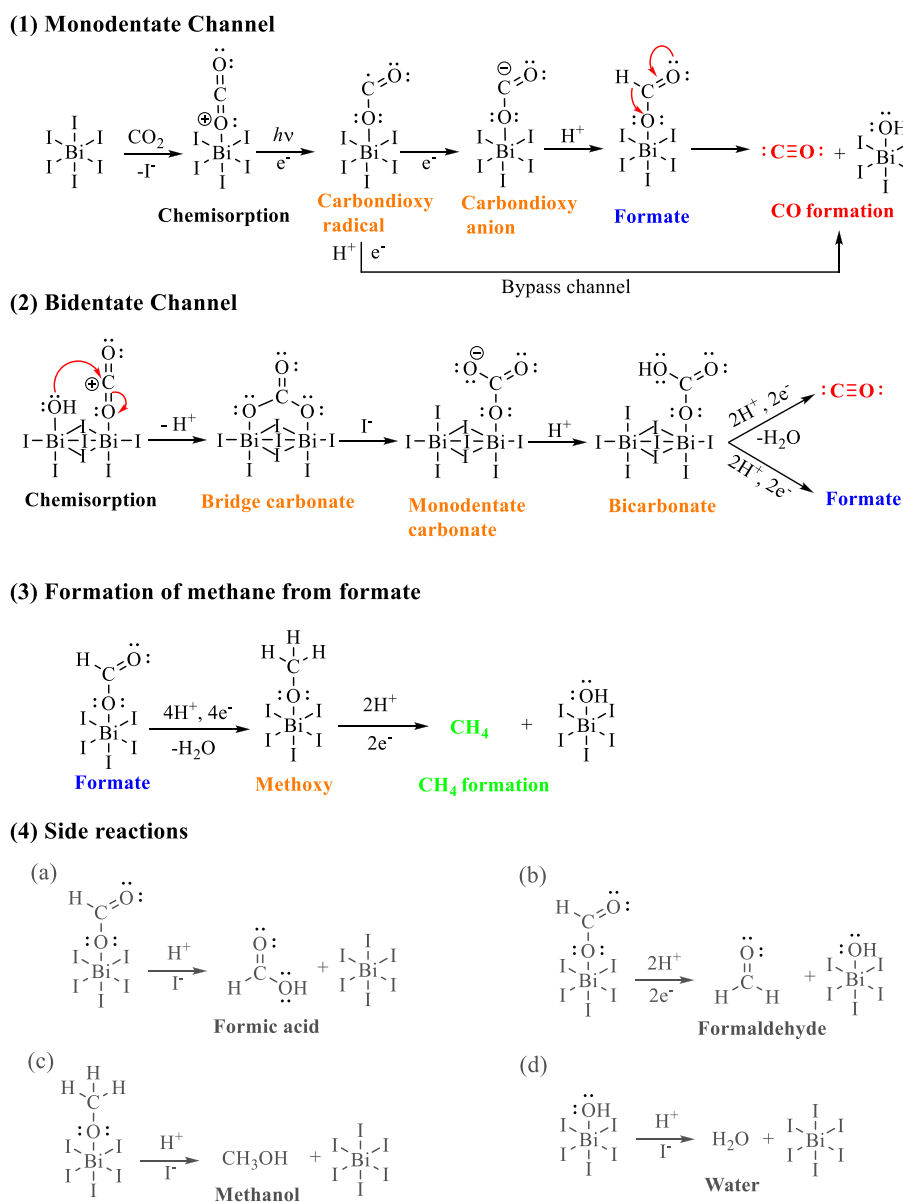ion on a scale of tens of nanoseconds, but its contribution ($\sim$0.04) was small for all three samples because of significant contributions from bulk trap-state relaxation (τ_1) and surface defect-state recombination (τ_2). As a result, the overall average PL lifetimes (τ_{PL}) show the trend $Rb_3Bi_2I_9 > Cs_3Bi_2I_9 > MA_3Bi_2I_9$.

Before proceeding toward photocatalytic reduction of carbon dioxide, we tested the stability of PeNC films in severe conditions of humidity and illumination. We compared the XRD patterns of fresh samples (Figure S4, SI) with the patterns of samples kept for 7 days in ambient conditions, RH = 70%. The same samples, after 7 days of aging, were illuminated with a UV lamp (80.4 μW cm^{-2}) for 12 h. No significant change was observed in the XRD patterns, especially

for PeNCs with inorganic cations. We thus conclude that the PeNCs were stable during the period of photoreduction.

Bi-based materials such as as bismuth oxyhalides have been extensively used in photocatalytic and electrocatalytic reduction of CO_2.[35−37] The incorporation of defects in the material to enhance the photocatalytic activity was observed such that defects increased the adsorption of CO_2 and trapping of excited electrons.[37−39] The crystal structure of the catalyst is another factor to be considered to improve its photocatalytic activity.[40] According to this criterion Bi-based defect halide perovskites ($A_3M_2X_9$) that form zero-dimensional and monoclinic crystals[32] are excellent candidates for photocatalytic reduction of CO_2. We applied Bi-based PeNCs as photocatalysts to investigate the reduction of CO_2 at a gas−solid interface, whereas a gas−liquid interface faces problems of limited solubility of CO_2 and detrimental products produced via photoreaction of the solvent molecules. For instance, the most commonly used solvent, ethyl ethanoate, can be decomposed into CO and CH_4 via its own photoreaction with UV light.[41] The ultraviolet photoelectron spectral data in

Figure S5, SI, indicate that the energy levels of all three PeNCs are suitable for CO_2 reduction.[36,42] In our experiments, we loaded the PeNCs, as prepared, at the bottom of a quartz reactor. N_2 gas was passed for 60 min to remove air and to ensure that the reaction system was under anaerobic conditions. CO_2 (99.9%) was bubbled through water to generate a mixture of CO_2 and H_2O vapor. A lamp (32W UV B, 305 nm) served as a light source with an intensity of 80.4 μW cm^{-2} to reduce CO_2 in a batch reactor (Figure S6, SI). The gaseous products in the photoreactor were analyzed at 1 h intervals with a gas chromatograph (GC). With a flame ionization detector (FID), the detection of carbon monoxide was impracticable; for this reason, only product yields of methane were determined as a function of duration of irradiation from 0 to 10 h; the results appear in Figure 4a.

Figures S7—S9, SI, show the GC-MS results of the three PeNCs. The retention periods for the formation of methane and CO are about 3.6 and 4.7 min, respectively. For the mass spectra, the major signals at m/z 16.1 and 28.1 are assigned to CH_4 and CO, respectively. Figure 4b shows the amounts of methane and carbon monoxide produced via UV irradiation for a period of 10 h and detected with GC-MS. The greatest yield of methane, 17.0 ± 1.6 μmol g^{-1}, was observed for $Rb_3Bi_2I_9$ PeNC, whereas 14.9 ± 0.8 and 9.8 ± 0.6 μmol g^{-1} were observed for $Cs_3Bi_2I_9$ and $MA_3Bi_2I_9$ PeNCs, respectively. CO was detected in the reaction system via GC-MS; the formation of CO attained the greatest level for $Cs_3Bi_2I_9$ PeNC (77.6 μmol g^{-1}); only 18.2 and 7.2 μmol g^{-1} were observed for $Rb_3Bi_2I_9$ and $MA_3Bi_2I_9$, respectively. It is remarkable to note that the formation yield of CO using $Cs_3Bi_2I_9$ PeNC has reached a new record as compared to those using the other photocatalysts summarized in Table S2, SI.

We carried out GC-MS studies for the following two points. First, the product yields were compared with those of P25 TiO_2, which serves as a standard for the photoreduction of CO_2 to form methane.[2] All Bi-based PeNCs acted as superior photocatalysts, producing methane 10—20 times as great as that of P25. Second, we undertook three control experiments to confirm that CH_4 and CO were produced from CO_2 photoreduction: (i) reaction in the presence of catalyst, CO_2, and water in dark conditions; (ii) reaction with catalyst and water under irradiation but in the absence of CO_2; (iii) reaction with CO_2 and water under irradiation but in the absence of catalyst. No photoproducts were detected in these three control experiments. For example, Figure S10a—c, SI, show the GC-MS results under condition (ii) for catalysts $Rb_3Bi_2I_9$, $Cs_3Bi_2I_9$, and $MA_3Bi_2I_9$, respectively. In the absence of CO_2, no photoproduct was observed, indicating that no photodegradation of the organic ligands surrounding the PeNC catalysts occurred during the period of illumination. Control experiments were also undertaken for CO_2 reduction at a gas—liquid interface using ethyl ethanoate as solvent.[19,20,26] Our results indicated that large amounts of methane and carbon monoxide for the system were produced in the absence of CO_2 and photocatalyst PeNC under illumination at 305 nm for 10 h. Figure S11, SI, shows the GC-MS results for these control experiments, which show clearly that ethyl ethanoate solvent can undergo photodegradation to form methane and carbon monoxide. Ethyl ethanoate is hence unsuitable for use in the gas—liquid reaction, whereas the gas—solid reaction is appropriate to study photocatalytic reduction of CO_2.

EPR spectra were recorded for samples in toluene solution at 77 K for each catalyst under illumination in the presence or absence of CO_2 and H_2O vapors to examine charge trapping and interfacial charge transfer. Figure 5 shows the EPR data in vacuum (solid curves) and in the presence of CO_2 and H_2O (dashed curves). As suitable EPR references were unavailable for lead-free perovskites, we compared the derivative signals of Bi perovskite EPR spectra with those of lead halide and organic lead halide perovskites.[43] According to the EPR spectra of a lead halide, electrons and holes are trapped by lead cations; the Pb^{3+} cation can stabilize holes to become EPR-active. Electrons are trapped in an EPR-inactive species. In an organic lead halide perovskite, electrons are trapped by the Pb^{2+} species to become EPR-inactive, whereas the EPR-active holes are trapped by the Pb^{3+} species and the organic cations.[43] Accordingly, the EPR results shown in Figure 5 indicate the amounts of EPR-active holes under illumination with the trend $Cs_3Bi_2I_9 > Rb_3Bi_2I_9 > MA_3Bi_2I_9$ in the absence of CO_2 and H_2O. When CO_2 and H_2O vapor was added to the system, the reduction of CO_2 in the presence of H_2O proceeded to quench the EPR-active holes with the same trend of photoactivity as that of EPR activity shown in Figure 5. As a control experiment, Figure S12, SI, shows the enhanced EPR activity when the three PeNC catalysts were exposed to light compared to their dark conditions. Our results indicate that $Cs_3Bi_2I_9$ exhibits a superior ability to generate electron and hole pairs relative to the other PeNCs. In general, Bi-based perovskites are expected to accept defect-tolerant electronic structures in which the conduction and valence bands are formed with antibonding orbitals.[44] Similar to the effect of lead perovskites, we expect that Bi-based perovskites can stabilize excited electrons with Bi^{3+} and holes with Bi^{4+} as in the cases of AgX and PbX_2 crystals (X represents a halide).[43]

EPR spectra were recorded also in the absence of ligands to clarify that the EPR signals are generated from the active holes upon irradiation. Figure S13a—d, SI, show no EPR signal from bulk perovskites and BiI_3 other than $MA_3Bi_2I_9$ (Figure S13c), indicating that quenching is more rapid in the absence of ligands for bulk $Rb_3Bi_2I_9$, $Cs_3Bi_2I_9$, and BiI_3.[30] In contrast, bulk $MA_3Bi_2I_9$ displays intense EPR signals attributed to $^\bullet CH_2NH_3^+$ radicals that represent trapping of holes by this organic cation.[43] In Figure 5, a g-factor of 2.002 indicates that the holes can be stabilized by Bi^{4+}; the presence of hyperfine splitting in the EPR signals was due to the unpaired electrons located on oxygen ions of the oleic acid.[45] According to our observation of $Rb_3Bi_2I_9$ and $Cs_3Bi_2I_9$, holes are efficiently stabilized by Bi^{4+} and oxygen ions, but, for $MA_3Bi_2I_9$, holes are stabilized by Bi^{4+}, $^\bullet CH_2NH_3^+$ radical cations, and oxygen anions. The transfer of the holes into water (the oxidation channel) is hence inefficient for MA-based PeNC, which results in decreased quenching of the EPR signal shown in Figure 5c. This effect has made $MA_3Bi_2I_9$ a poorer photocatalyst than the other two PeNC catalysts, consistent with the results shown in Figure 4. In addition, $Cs_3Bi_2I_9$ PeNC exhibits the greatest photocatalytic activity because of its superior charge generation and efficient charge transfer in the presence of CO_2 and H_2O. The crystal structure of $Cs_3Bi_2I_9$ can also support its high catalytic activity. $Rb_3Bi_2I_9$ adopts a crystal structure of distorted-defect variant perovskite type ($A_3M_2X_9$), for which every third M layer of the perovskite in facet [001] is depleted.[32] As bismuth constitutes the active site of the catalyst, the depletion of bismuth in $Rb_3Bi_2I_9$ thus decreases the photocatalytic activity relative to $Cs_3Bi_2I_9$.

We recorded diffuse-reflectance infrared spectra to understand the reaction mechanism for CO_2 reduction using PeNC in this series as photocatalysts. These spectra were recorded under diffuse-reflection conditions; the surface-adsorbed chemical species were analyzed through examination of the infrared signals following illumination. The illumination time was varied to study intermediate steps in the catalytic process, with results shown in Figure S14, SI. Figure 6 shows spectra after illumination for 300 min for the three catalysts with various steady-state intermediate species labeled as indicated in the caption.

Bands (a) and (b) in the spectra show free OH and H-bonded OH vibrations, respectively, but only $Rb_3Bi_2I_9$ displays the free OH vibrational feature because of its layer-defect crystal structure. Upon photoreduction of CO_2, the surfaces of these PeNC catalysts became covered with the hydroxyl group, thus exhibiting a hydrophilic property. The intermediate species shown in Figure 6 provide crucial evidence for the photocatalytic reaction. First, the pronounced formation of lines (e) and (c) in $Rb_3Bi_2I_9$ indicates that dioxycarbon anion and formate might be the most significant intermediates for CO_2 reduction and that the mechanism occurs via the monodentate channel shown in Figure 7a. In contrast, for $Cs_3Bi_2I_9$, spectral lines (d), (f), and (j) corresponded to the formation of bridge carbonate, monodentate carbonate, and bidentate carbonate, respectively. The CO_2 reduction with a $Cs_3Bi_2I_9$ PeNC catalyst might hence follow a bidentate channel shown in Figure 7b. Second, in both monodentate and bidentate channels, formate is the key intermediate for the photoreduction of CO_2 to form both CO and methane. The formation of methane is an eight-electron process from CO_2; the reaction mechanism to form methane from formate is shown in Figure 7c. As a result, the infrared intensity of formate shows the trend $Rb_3Bi_2I_9$ > $Cs_3Bi_2I_9$ > $MA_3Bi_2I_9$, which is consistent with the trend of the methane product yields shown in Figure 4. Third, the side reactions for the formation of formic acid (a two-electron process), formaldehyde (a four-electron process), and methanol (a six-electron process) are shown in Figure 7d. As we observed no side product in our GC-MS system, these side reactions were dark; the formation of only CO and methane was observed, as discussed above.

Our Bi-based PeNCs were composed of corner-sharing BiI_6 octahedra; these octahedra are situated at the surface of PeNC to facilitate the attachment of ligands OA and OLA.[29,31] BiI_6 acts as a Lewis acid and forms a donor−acceptor complex with CO_2, which results in chemisorption of CO_2 from the oxygen side. CO is the primary product, which requires only two electrons to form via either a monodentate or a bidentate channel shown in Figure 7. We emphasize that $Cs_3Bi_2I_9$ exhibited the best photocatalytic activity (Figure 6), which is consistent with the greatest product yield of CO formation (Figure 4b) for this catalyst. As the major path for formation of CO and methane is via the bidentate channel for $Cs_3Bi_2I_9$, the large amount of CO might be produced via the monodentate channel through the dioxycarbon radical bypass channel shown in Figure 7a. This inference is based on the appearance of the dioxycarbon anion intensity, which is smaller for $Cs_3Bi_2I_9$ than for $Rb_3Bi_2I_9$. Both monodentate and bidentate channels contribute to the formation of CO for $Cs_3Bi_2I_9$, as rationalized for its large yield of CO mentioned above.

CONCLUSION

We demonstrated a novel top-down synthetic method via ultrasonication to make three bismuth-based PeNC materials and have shown their potential application in the photoreduction of carbon dioxide at the gas−solid interface to generate carbon monoxide and methane as products. We analyzed the photoproducts and conducted control experiments with a gas chromatograph and a mass spectrometer. The yields of product CO exhibit the trend $Cs_3Bi_2I_9 \gg Rb_3Bi_2I_9 > MA_3Bi_2I_9 \gg TiO_2$, whereas those of methane show the trend $Rb_3Bi_2I_9 > Cs_3Bi_2I_9 > MA_3Bi_2I_9 \gg TiO_2$. EPR and diffuse-reflectance infrared spectra were recorded to explain the varied photocatalytic activity of these three PeNC photocatalysts. A superior charge transfer in $Cs_3Bi_2I_9$ and restricted charge transport in $MA_3Bi_2I_9$ were deduced from the EPR results. From a careful analysis of the infrared spectra we propose a complete reaction mechanism for the reduction of CO_2 using Bi-based PeNC catalysts to rationalize the observed trends of the yields of both CO and methane. These Bi-based PeNCs have large band gaps in the visible region with great binding energies so that they may have the potential to serve in other optoelectronic applications.

ASSOCIATED CONTENT

Ⓢ Supporting Information

The Supporting Information is available free of charge at https://pubs.acs.org/doi/10.1021/jacs.9b11089.

Experimental details, 14 supplementary figures, and two supplementary tables (PDF)

AUTHOR INFORMATION

Corresponding Author

*diau@mail.nctu.edu.tw

ORCID Ⓘ

Eric Wei-Guang Diau: 0000-0001-6113-5679

Notes

The authors declare no competing financial interest.

ACKNOWLEDGMENTS

REFERENCES

(1) Bae, K. L.; Kim, J.; Lim, C. K.; Nam, K. M.; Song, H. Colloidal Zinc Oxide-Copper(I) Oxide Nanocatalysts for Selective Aqueous Photocatalytic Carbon Dioxide Conversion into Methane. *Nat. Commun.* **2017**, *8*, 1156−1173.

(2) Yu, J.; Low, J.; Xiao, W.; Zhou, P.; Jaroniec, M. Enhanced Photocatalytic CO_2-Reduction Activity of Anatase TiO_2 by Coexposed {001} and {101} Facets. *J. Am. Chem. Soc.* **2014**, *136*, 8839−8842.

(3) Cao, S.; Tao, F. F.; Tang, Y.; Li, Y.; Yu, J. Size- and Shape-Dependent Catalytic Performances of Oxidation and Reduction Reactions on Nanocatalysts. *Chem. Soc. Rev.* **2016**, *45*, 4747−4765.

(4) Roy, S.; Rao, A.; Devatha, G.; Pillai, P. P. Revealing the Role of Electrostatics in Gold-Nanoparticle-Catalyzed Reduction of Charged Substrates. *ACS Catal.* **2017**, *7*, 7141−7145.

(5) Jokar, E.; Chien, C. H.; Fathi, A.; Rameez, M.; Chang, Y. H.; Diau, E. W. G. Slow Surface Passivation and Crystal Relaxation with Additives to Improve Device Performance and Durability for Tin-Based Perovskite Solar Cells. *Energy Environ. Sci.* **2018**, *11*, 2353−2362.

(6) Jokar, E.; Chien, C. H.; Tsai, C. M.; Fathi, A.; Diau, E. W. G. Robust Tin-Based Perovskite Solar Cells with Hybrid Organic Cations to Attain Efficiency Approaching 10%. *Adv. Mater.* **2019**, *31*, 1804835.

(7) Diau, E. W.-G.; Jokar, E.; Rameez, M. Strategies to Improve Performance and Stability for Tin-Based Perovskite Solar Cells. *ACS Energy Lett.* **2019**, *4*, 1930−1937.

(8) Tan, Z. K.; Moghaddam, R. S.; Lai, M. L.; Docampo, P.; Higler, R.; Deschler, F.; Price, M.; Sadhanala, A.; Pazos, L. M.; Credgington, D.; Hanush, F.; Bein, T.; Snaith, H. J.; Friend, R. H. Bright Light-Emitting Diodes Based on Organometal Halide Perovskite. *Nat. Nanotechnol.* **2014**, *9*, 687−692.

(9) Xiao, Z.; Kerner, R. A.; Zhao, L.; Tran, N. L.; Lee, K. M.; Koh, T.-W.; Scholes, G. D.; Rand, B. P. Efficient Perovskite Light-Emitting Diodes Featuring Nanometre-Sized Crystallites. *Nat. Photonics* **2017**, *11*, 108−115.

(10) Naphade, R.; Zhao, B.; Richter, J. M.; Booker, E.; Friend, R.; Sadhanala, A.; Ogale, S. High Quality Hybrid Perovskite Semiconductor Thin-Films with Remarkably Enhanced Luminescence and Defect Suppression via Quaternary Alkyl Ammonium Salts Based Treatment. *Adv. Mater. Interfaces* **2017**, *4*, 1700562−1700569.

(11) Byun, J.; Cho, H.; Wolf, C.; Jang, M.; Sadhanala, A.; Friend, R. H.; Yang, H.; Lee, T. W. Efficient Visible Quasi-2D Perovskite Light-Emitting Diodes. *Adv. Mater.* **2016**, *28*, 7515−7520.

(12) Cho, H.; Jeong, S.-H.; Park, M.-H.; Kim, Y.-H.; Wolf, C.; Lee, C.-L.; Heo, J. H.; Sadhanala, A.; Myoung, N.; Yoo, S.; Im, S. H.; Friend, R. H.; Lee, T. W. Overcoming the Electroluminescence Efficiency Limitations of Perovskite Light-Emitting Diodes. *Science* **2015**, *350*, 1222−1225.

(13) Ji, L.; Hsu, H.-Y.; Lee, J.; Bard, A. J.; Yu, E. T. High Performance Photodetectors Based on Solution-Processed Epitaxial Grown Hybrid Halide Perovskites. *Nano Lett.* **2018**, *18*, 994−1000.

(14) Bai, F.; Qi, J.; Li, F.; Fang, Y.; Han, W.; Wu, H.; Zhang, Y. A High-Performance Self-Powered Photodetector Based on Monolayer MoS_2/Perovskite Heterostructures. *Adv. Mater. Interfaces* **2018**, *5*, 1701275−1701283.

(15) Stranks, S. D.; Wood, S. M.; Wojciechowski, K.; Deschler, F.; Saliba, M.; Khandelwal, H.; Patel, J. B.; Elston, S. J.; Herz, L. M.; Johnston, M. B.; Schenning, A. P. H. J.; Debije, M. G.; Riede, M. K.; Morris, S. M.; Snaith, H. J. Enhanced Amplified Spontaneous Emission in Perovskites Using a Flexible Cholesteric Liquid Crystal Reflector. *Nano Lett.* **2015**, *15*, 4935−4941.

(16) Pan, J.; Sarmah, S. P.; Murali, B.; Dursun, I.; Peng, W.; Parida, M. R.; Liu, J.; Sinatra, L.; Alyami, N.; Zhao, C.; Alarousu, E.; Ng, T. K.; Ooi, B. S.; Bakr, O. M.; Mohammed, O. F. Air-Stable Surface-Passivated Perovskite Quantum Dots for Ultra-Robust, Single- and Two-Photon-Induced Amplified Spontaneous Emission. *J. Phys. Chem. Lett.* **2015**, *6*, 5027−5033.

(17) Eaton, S. W.; Lai, M.; Gibson, N. A.; Wong, A. B.; Dou, L.; Ma, J.; Wang, L.-W.; Leone, S. R.; Yang, P. Lasing in Robust Cesium Lead Halide Perovskite Nanowires. *Proc. Natl. Acad. Sci. U. S. A.* **2016**, *113*, 1993−1998.

(18) Huang, H.; Polavarapu, L.; Sichert, J. A.; Susha, A. S.; Urban, A. S.; Rogach, A. L. Colloidal Lead Halide Perovskite Nanocrystals: Synthesis, Optical Properties and Applications. *NPG Asia Mater.* **2016**, *8*, e328−e342.

(19) Xu, Y. F.; Yang, M. Z.; Chen, B. X.; Wang, X. D.; Chen, H. Y.; Kuang, D. B.; Su, C. Y. A $CsPbBr_3$ Perovskite Quantum Dot/Graphene Oxide Composite for Photocatalytic CO_2 Reduction. *J. Am. Chem. Soc.* **2017**, *139*, 5660−5663.

(20) Hou, J.; Cao, S.; Wu, Y.; Gao, Z.; Liang, F.; Sun, Y.; Lin, Z.; Sun, L. Inorganic Colloidal Perovskite Quantum Dots for Robust Solar CO_2 Reduction. *Chem. - Eur. J.* **2017**, *23*, 9481−9485.

(21) Protesescu, L.; Yakunin, S.; Bodnarchuk, M. I.; Krieg, F.; Caputo, R.; Hendon, C. H.; Yang, R. X.; Walsh, A.; Kovalenko, M. V. Nanocrystals of Cesium Lead Halide Perovskites ($CsPbX_3$, X = Cl, Br, and I): Novel Optoelectronic Materials Showing Bright Emission with Wide Color Gamut. *Nano Lett.* **2015**, *15*, 3692−3696.

(22) Schmidt, L. C.; Pertegás, A.; González-Carrero, S.; Malinkiewicz, O.; Agouram, S.; Mínguez Espallargas, G.; Bolink, H. J.; Galian, R. E.; Pérez-Prieto, J. Nontemplate Synthesis of $CH_3NH_3PbBr_3$ Perovskite Nanoparticles. *J. Am. Chem. Soc.* **2014**, *136*, 850−853.

(23) Huang, H.; Xue, Q.; Chen, B.; Xiong, Y.; Schneider, J.; Zhi, C.; Zhong, H.; Rogach, A. L. Top-Down Fabrication of Stable Methylammonium Lead Halide Perovskite Nanocrystals by Employing a Mixture of Ligands as Coordinating Solvents. *Angew. Chem., Int. Ed.* **2017**, *56*, 9571−9576.

(24) Kong, Z.-C.; Liao, J.-F.; Dong, Y.-J.; Xu, Y.-F.; Chen, H.-Y.; Kuang, D.-B.; Su, C.-Y. Core@Shell $CsPbBr_3$@Zeolitic Imidazolate Framework Nanocomposite for Efficient Photocatalytic CO_2 Reduction. *ACS Energy Lett.* **2018**, *3*, 2656−2662.

(25) Jellicoe, T. C.; Richter, J. M.; Glass, H. F. J.; Tabachnyk, M.; Brady, R.; Dutton, S. E.; Rao, A.; Friend, R. H.; Credgington, D.; Greenham, N. C.; Bohm, M. L. Synthesis and Optical Properties of Lead-Free Cesium Tin Halide Perovskite Nanocrystals. *J. Am. Chem. Soc.* **2016**, *138*, 2941−2944.

(26) Zhou, L.; Xu, Y.-F.; Chen, B.-X.; Kuang, D.-B.; Su, C.-Y. Synthesis and Photocatalytic Application of Stable Lead-Free $Cs_2AgBiBr_6$ Perovskite Nanocrystals. *Small* **2018**, *14*, 1703762−1703768.

(27) Park, B. W.; Philippe, B.; Zhang, X.; Rensmo, H.; Boschloo, G.; Johansson, E. M. J. Bismuth Based Hybrid Perovskites $A_3Bi_2I_9$ (A: Methylammonium or Caesium) for Solar Cell Application. *Adv. Mater.* **2015**, *27*, 6806−6813.

(28) Jain, S. M.; Phuyal, D.; Davies, M. L.; Li, M.; Philippe, B.; De Castro, C.; Qiu, Z.; Kim, J.; Watson, T.; Tsoi, W. C.; Karis, O.; Rensmo, H.; Boschloo, G.; Edvinsson, T.; Durrant, J. R. An effective approach of vapour assisted morphological tailoring for reducing metal defect sites in lead-free, $(CH_3NH_3)_3Bi_2I_9$ Bismuth-based perovskite solar cells for improved performance and long-term stability. *Nano Energy* **2018**, *49*, 614−624.

(29) McCall, K. M.; Stoumpos, C. C.; Kostina, S. S.; Kanatzidis, M. G.; Wessels, B. W. Strong Electron-Phonon Coupling and Self-Trapped Excitons in the Defect Halide Perovskites $A_3M_2I_9$(A = Cs, Rb; M = Bi, Sb). *Chem. Mater.* **2017**, *29*, 4129−4145.

(30) Yang, B.; Chen, J.; Hong, F.; Mao, X.; Zheng, K.; Yang, S.; Li, Y.; Pullerits, T.; Deng, W.; Han, K. Lead-Free, Air-Stable All-Inorganic Cesium Bismuth Halide Perovskite Nanocrystals. *Angew. Chem., Int. Ed.* **2017**, *56*, 12471−12475.

(31) Leng, M.; Chen, Z.; Yang, Y.; Li, Z.; Zeng, K.; Li, K.; Niu, G.; He, Y.; Zhou, Q.; Tang, J. Lead-Free, Blue-emitting Bismuth Halide Perovskite Quantum Dots. *Angew. Chem., Int. Ed.* **2016**, *55*, 15012−15016.

(32) Lehner, A. J.; Fabini, D. H.; Evans, H. A.; Hébert, C. A.; Smock, S. R.; Hu, J.; Wang, H.; Zwanziger, J. W.; Chabinyc, M. L.; Seshadri, R. Crystal and Electronic Structures of Complex Bismuth Iodides $A_3Bi_2I_9$ (A = K, Rb, Cs) Related to Perovskite: Aiding the Rational Design of Photovoltaics. *Chem. Mater.* **2015**, *27*, 7137−7148.

(33) Scardi, P.; Leoni, M.; Beyerlein, K. R. On the Modelling of the Powder Pattern from a Nanocrystalline Material. *Z. Kristallogr.* **2011**, *226*, 924−933.

(34) Zhang, Y.; Yin, J.; Parida, M. R.; Ahmed, G. H.; Pan, J.; Bakr, O. M.; Brédas, J. L.; Mohammed, O. F. Direct-Indirect Nature of the Bandgap in Lead-Free Perovskite Nanocrystals. *J. Phys. Chem. Lett.* **2017**, *8*, 3173−3177.

(35) Lee, C. W.; Hong, J. S.; Yang, K. D.; Jin, K.; Lee, J. H.; Ahn, H.-Y.; Seo, H.; Sung, N.-E.; Nam, K. T. Selective Electrochemical

Production of Formate from Carbon Dioxide with Bismuth-Based Catalysts in an Aqueous Electrolyte. *ACS Catal.* **2018**, *8*, 931−937.

(36) Zhang, L.; Wang, W.; Jiang, D.; Gao, E.; Sun, S. Photoreduction of CO_2 on BiOCl Nanoplates with the Assistance of Photoinduced Oxygen Vacancies. *Nano Res.* **2015**, *8*, 821−831.

(37) Kong, X. Y.; Lee, W. P. C.; Ong, W. J.; Chai, S. P.; Mohamed, A. R. Oxygen-Deficient BiOBr as a Highly Stable Photocatalyst for Efficient CO_2 Reduction into Renewable Carbon-Neutral Fuels. *ChemCatChem* **2016**, *8*, 3074−3081.

(38) Jiao, X.; Chen, Z.; Li, X.; Sun, Y.; Gao, S.; Yan, W.; Wang, C.; Zhang, Q.; Lin, Y.; Luo, Y.; Xie, Y. Defect-Mediated Electron-Hole Separation in One-Unit-Cell $ZnIn_2S_4$ Layers for Boosted Solar-Driven CO_2 Reduction. *J. Am. Chem. Soc.* **2017**, *139*, 7586−7594.

(39) Chang, X.; Wang, T.; Gong, J. CO_2 photo-Reduction: Insights into CO_2 activation and Reaction on Surfaces of Photocatalysts. *Energy Environ. Sci.* **2016**, *9*, 2177−2196.

(40) Habisreutinger, S. N.; Schmidt-Mende, L.; Stolarczyk, J. K. Photocatalytic Reduction of CO_2 on TiO_2 and Other Semiconductors. *Angew. Chem., Int. Ed.* **2013**, *52*, 7372−7408.

(41) Zhao, Y.; Sun, X.; Wang, W.; Xu, L. Quantum Chemical Study on the Atmospheric Photooxidation of Ethyl Acetate. *Can. J. Chem.* **2014**, *92*, 814−820.

(42) Lyu, M.; Yun, J. H.; Cai, M.; Jiao, Y.; Bernhardt, P. V.; Zhang, M.; Wang, Q.; Du, A.; Wang, H.; Liu, G.; Wang, L. Organic−Inorganic Bismuth (III)-Based Material: A Lead-Free, Air-Stable and Solution-Processable Light-Absorber beyond Organolead Perovskites. *Nano Res.* **2016**, *9*, 692−702.

(43) Shkrob, I. A.; Marin, T. W. Charge Trapping in Photovoltaically Active Perovskites and Related Halogenoplumbate Compounds. *J. Phys. Chem. Lett.* **2014**, *5*, 1066−1071.

(44) Lee, L. C.; Huq, T. N.; Macmanus-Driscoll, J. L.; Hoye, R. L. Z. Research Update: Bismuth-Based Perovskite-Inspired Photovoltaic Materials. *APL Mater.* **2018**, *6*, 084502−084517.

(45) Murphy, H. J.; Stevens, K. T.; Garces, N. Y.; Moldovan, M.; Giles, N. C.; Halliburton, L. E. Optical and EPR Characterization of Point Defects in Bismuth-Doped $CdWO_4$ Crystals. *Radiat. Eff. Defects Solids* **2007**, *149*, 273−278.

(46) Tang, C.; Feng, Z.; Liu, H.; An, H.; Li, G.; Wang, J.; Li, C.; Li, Z.; Liu, T. A Highly Selective and Stable ZnO-ZrO_2 Solid Solution Catalyst for CO_2 Hydrogenation to Methanol. *Sci. Adv.* **2017**, *3*, e1701290−e1701299.

(47) Yin, G.; Huang, X.; Chen, T.; Zhao, W.; Bi, Q.; Xu, J.; Han, Y.; Huang, F. Hydrogenated Blue Titania for Efficient Solar to Chemical Conversions: Preparation, Characterization, and Reaction Mechanism of CO_2 Reduction. *ACS Catal.* **2018**, *8*, 1009−1017.

(48) Liu, L.; Zhao, H.; Andino, J. M.; Li, Y. Photocatalytic CO_2 Reduction with H_2O on TiO_2 Nanocrystals: Comparison of Anatase, Rutile, and Brookite Polymorphs and Exploration of Surface Chemistry. *ACS Catal.* **2012**, *2*, 1817−1828.

(49) Yang, C. C.; Yu, Y. H.; Van Der Linden, B.; Wu, J. C. S.; Mul, G. Artificial Photosynthesis over Crystalline TiO_2-Based Catalysts: Fact or Fiction? *J. Am. Chem. Soc.* **2010**, *132*, 8398−8406.

(50) Martra, G. Lewis Acid and Base Sites at the Surface of Microcrystalline Anatase. *Appl. Catal., A* **2000**, *200*, 275−285.

(51) Wu, W.; Bhattacharyya, K.; Gray, K.; Weitz, E. Photoinduced Reactions of Surface-Bound Species on Titania Nanotubes and Platinized Titania Nanotubes: An in Situ FTIR Study. *J. Phys. Chem. C* **2013**, *117*, 20643−20655.

(52) Luo, C.; Zhao, J.; Li, Y.; Zhao, W.; Zeng, Y.; Wang, C. Photocatalytic CO_2 Reduction over $SrTiO_3$: Correlation between Surface Structure and Activity. *Appl. Surf. Sci.* **2018**, *447*, 627−635.

(53) Bashir, S.; Idriss, H. Mechanistic Study of the Role of Au, Pd and Au-Pd in the Surface Reactions of Ethanol over TiO_2 in the Dark and under Photo-Excitation. *Catal. Sci. Technol.* **2017**, *7*, 5301−5320.